

Search for Dark Matter Candidates Produced in  $Z(\ell\ell) + E_{\text{T}}^{\text{miss}}$  Events in 13 TeV  
Proton-Proton Collisions with the ATLAS Detector at the Large Hadron Collider

by

Kayla McLean

B.Sc., University of Victoria, 2014

A Proposal Submitted in Partial Fulfillment of the  
Requirements for the Candidacy of

DOCTOR OF PHILOSOPHY

in the Department of Physics and Astronomy

University of Victoria

# Contents

<b>Table of Contents</b>	<b>ii</b>
<b>1 Introduction</b>	<b>1</b>
<b>2 Dark Matter Searches with the ATLAS Detector</b>	<b>4</b>
2.1 Dark Matter Theory . . . . .	4
2.2 The LHC and the ATLAS Detector . . . . .	7
<b>3 The Mono-<math>Z(\ell\ell)</math> Search</b>	<b>10</b>
3.1 Analysis Overview . . . . .	10
3.2 Truth Studies . . . . .	12
3.3 Estimation of the $Z$ +jets Background . . . . .	14
3.3.1 ABCD Method . . . . .	14
3.3.2 $\gamma$ +jets Technique . . . . .	16
3.4 Dark Matter Limit Setting . . . . .	18
3.5 Analysis Software . . . . .	22
<b>4 Analysis with the Full Run 2 Dataset</b>	<b>23</b>
4.1 Event Selection Optimization . . . . .	23
4.2 Development of the $\gamma$ +jets Technique . . . . .	25
4.3 Signal Models . . . . .	26
4.4 Other Analysis Improvements . . . . .	29
<b>5 Conclusions</b>	<b>32</b>
<b>A Appendix</b>	<b>33</b>
A.1 Event Selections . . . . .	33
A.2 Calibration Studies on Close-By Jets . . . . .	34
<b>Bibliography</b>	<b>35</b>

# Chapter 1

## Introduction

The Standard Model (SM) of particle physics is the most complete theory that exists to describe elementary particles and their interactions. However there are known weaknesses in the SM, one of which is the failure to include a description of dark matter (DM). There is strong evidence from astronomical observations that there is a large excess of matter in the universe that appears to have only gravitational interactions with SM particles. Some examples for the evidence of dark matter include measurements of rotation velocities of spiral galaxies, gravitational lensing effects, and anisotropies in the cosmic microwave background. The standard model of cosmology predicts that dark matter accounts for more than 80% of the total matter in the universe. Although there are many theories to describe possible dark matter candidates, the one of interest here is the WIMP (weakly interacting massive particle). The WIMP is a Dirac fermion, often denoted  $\chi$ , and is predicted to interact gravitationally and through other force(s), potentially beyond the SM. It is believed to have a mass between  $\mathcal{O}(1)$  GeV and  $\mathcal{O}(100)$  TeV and have a self-annihilation cross section similar to that of SM weak interactions [1].

There are three categories of experiments that have potential to observe dark matter: direct detection, indirect detection, and collider production. Figure 1.1 shows a schematic that illustrates their complementarity to one another. Direct detection experiments attempt to observe recoils in SM particles from scattering with dark matter. Indirect detection experiments measure decay products from DM annihilation. Collider experiments look for dark matter that is produced from the interaction of SM particles. This work focuses on the production of dark matter at the Large Hadron Collider (LHC) using data collected from proton-proton ( $pp$ ) collisions inside the ATLAS detector.

If it is possible to produce dark matter in collisions of SM particles, then an additional complication is how the presence of dark matter can be determined in the complex events

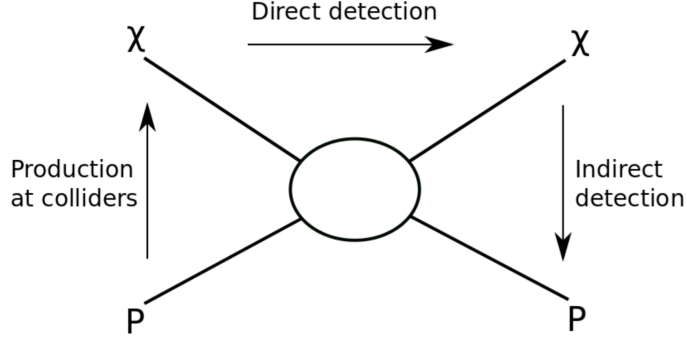


Figure 1.1: Schematic of dark matter searches [2].

of high energy particles. Collider experiments use a quantity known as *missing transverse momentum*, commonly denoted  $\vec{E}_T^{\text{miss}}$ , to quantify the amount of invisible decay products in collisions. Its magnitude,  $E_T^{\text{miss}}$ , is known as missing transverse energy. The plane perpendicular to the beam axis, also known as the transverse plane, is of particular importance in collider experiments. Before colliding, the protons in the beam only move along the beam axis, so the net momentum in the transverse plane is zero. From conservation of momentum, the net transverse momentum after the collision therefore must also be zero. If the transverse momenta of all visible particles produced in the collision are added together vectorially, they should add to zero. But, if invisible particles are present, such as neutrinos or dark matter, then the sum will instead add to a non-zero transverse momentum vector. We therefore infer that there are non-interacting particles produced, and they have a net  $\vec{E}_T^{\text{miss}}$  that is the negative of the vectorial sum of the transverse momenta of the visible particles. Hence a dark matter signal would manifest as an excess of collision events with a significant amount of  $E_T^{\text{miss}}$  compared to the SM prediction.

Mono- $X$  searches study a certain phenomenology of dark matter where a visible particle,  $X$ , is used as a ‘tag.’ If the amount of missing energy in an event is large, the tag particle will experience a significant amount of recoil against the  $\vec{E}_T^{\text{miss}}$ . This gives a mean of identifying potentially interesting events. In this work the  $Z$  boson is used as a tag, which is identified in events from a pair of same sign, opposite charge leptons ( $e^+e^-$  or  $\mu^+\mu^-$ ). Hence this analysis attempts to find dark matter with  $Z(\ell\ell) + E_T^{\text{miss}}$  events, and is therefore commonly referred to as the mono- $Z(\ell\ell)$  search. Other mono- $X$  searches use different SM particles as tags, such as a jet, photon,  $W$ , or the Higgs.

The ATLAS experiment has been in a period of intense data-taking since the start of Run 2 in 2015, with  $pp$  collisions at a centre-of-mass energy of 13 TeV. As data continues to

be collected until the end of 2018, the discovery potential for dark matter at the LHC has never been higher. This document summarizes the work done on the mono- $Z(\ell\ell)$  analysis so far as well as the prospects using the full Run 2 dataset. Chapter 2 includes a summary of the dark matter models considered in the analysis, as well as a brief description of the LHC and the ATLAS detector. Chapter 3 covers the details of the search with a focus on the work done for the results obtained using the 2015 and 2015+2016 datasets. Chapter 4 describes the plan to analyze the complete Run 2 dataset corresponding to the full 2015-2018 period.

## Chapter 2

# Dark Matter Searches with the ATLAS Detector

### 2.1 Dark Matter Theory

Effective field theories (EFTs) [3] [4] were the primary models studied in  $E_T^{\text{miss}} + X$  dark matter searches in Run 1, when the centre-of-mass energy was 8 TeV. In short, these theories assume that a dark matter pair is produced by means of a contact interaction with a quark and antiquark, as illustrated in Figure 2.1. These types of models offer a straightforward means to compare collider results to direct or indirect detection experiments. However, EFTs are only valid when the mass of the mediating particle between the  $\chi\bar{\chi}$  and  $q\bar{q}$  is much heavier than the momentum transfer of the process. Now that the centre-of-mass energy has increased to 13 TeV in Run 2, these EFTs are no longer valid. Thus, a new baseline model is used in Run 2 with the mediator particle explicitly included.

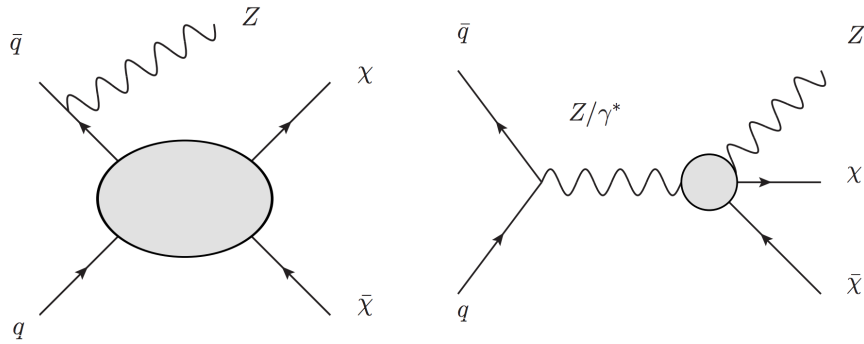


Figure 2.1: Representative EFT diagrams for the mono- $Z$  signature [4].

Leading order simplified models are the first set of benchmark models used for  $E_T^{\text{miss}} + X$  searches in Run 2, as recommended by the LHC DM Working Group [3]. An example  $s$ -channel diagram for the  $E_T^{\text{miss}} + Z$  signal is shown in Figure 2.2. These models are considered ‘simplified’ because they introduce the minimum number of parameters needed to include a mediator between SM and dark matter particles (compared to more complicated models such as supersymmetry).

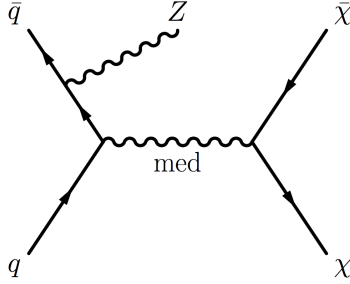


Figure 2.2: Simplified model  $s$ -channel diagram for the mono- $Z$  signature [5].

Simplified models introduce five new parameters: the mass of the WIMP,  $m_\chi$ , the mass of the mediating particle,  $m_{\text{med}}$ , the couplings of the mediator to the SM (to dark matter),  $g_q$  ( $g_\chi$ ), and the width of the mediator  $\Gamma_{\text{med}}$ . The mediator particle can be spin-0 (scalar or pseudo-scalar) or spin-1 (vector or axial-vector).

Following the recommendations in Ref. [3], for spin-0 models the couplings are set to  $g_q = g_\chi = 1.0$ . The Yukawa couplings are also included between the quarks and the mediator. For spin-1 models the couplings are fixed to  $g_q = 0.25$  and  $g_\chi = 1.0$ . In addition, assuming that the mediator has no additional decay modes,  $\Gamma_{\text{med}}$  is set to the minimal width [6], which is fixed by  $g_q$ ,  $g_\chi$ ,  $m_\chi$ , and  $m_{\text{med}}$ . The couplings were chosen so that  $\Gamma_{\text{med}}/m_{\text{med}} < \sim 0.05$ , and to correspond approximately to an estimate of the lower sensitivity of the Run 2 mono-jet analysis.

Run 2 mono- $X$  analyses have adopted the  $s$ -channel exchange of an axial-vector mediator as the primary benchmark scenario. This choice is motivated by the findings in Ref. [3] that show that collider searches can be more sensitive than direct detection experiments at low values of  $m_\chi$  for this type of mediator.

Although they have advantages compared to EFTs, simplified models are not a complete theory and violate unitarity for some regions of parameter space. At the beginning of Run 2 they were useful in providing a guideline for the ATLAS and CMS collaborations to follow in tandem, but there is now interest in studying richer, more theoretically complete models.

A popular model in Run 2 mono- $X$  dark matter searches is known as the two Higgs

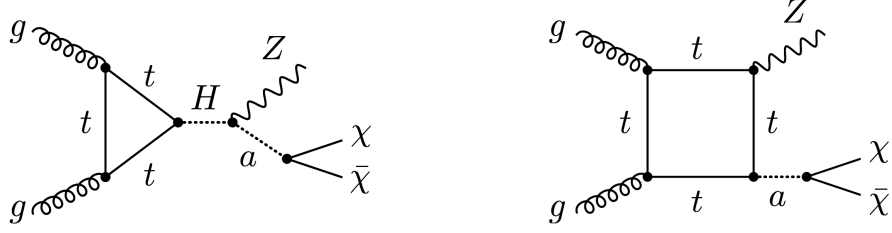


Figure 2.3: 2HDM+PS diagrams for the mono- $Z$  signature produced by  $gg$  fusion [7]. The second diagram can have  $A$  in place of  $a$ .

doublet + pseudo-scalar (2HDM+PS) model [7]. The addition of another  $SU(2)$  doublet to the SM is essential for many well-motivated BSM theories [8]. 2HDM models are also perturbative, and avoid violating unitarity by allowing mixing between the dark matter mediator and other bosons.

Figure 2.3 shows the two main diagrams of the 2HDM+PS model with the mono- $Z$  signature. This model has two CP-even scalars  $h$  and  $H$  (where  $h$  is the SM Higgs with  $m_h = 125$  GeV and  $m_H > m_h$ ), one CP-odd pseudo-scalar  $A$ , two charged scalars  $H^+$  and  $H^-$ , and the pseudo-scalar  $a$  that couples the SM to dark matter. There are also the parameters  $\sin(\beta - \alpha)$  and  $\tan \beta$ , where  $\alpha$  is the mixing angle between  $h$  and  $H$ , and  $\tan \beta$  is the ratio of their vacuum expectation values. The parameters are chosen to have  $m_A = m_H = m_{H^\pm}$ .

Such models are of great interest to the mono- $Z$  search because the mono- $Z$  signature has better sensitivity than mono-jet for some regions of phase space. This is not the case for simplified models, where the mono-jet analysis always has higher sensitivity. In addition, there are couplings between  $H$  and the  $Z$  that are unique to the mono- $Z$  search.

So far the mono- $Z$  analysis has excluded a range of signals from the simplified and 2HDM+PS models. Prospective models to be studied with the full Run 2 dataset will be discussed in Chapter 4, including coloured scalar mediator ( $t$ -channel) signatures and so-called Less Simplified models.



## 2.2 The LHC and the ATLAS Detector

The Large Hadron Collider (LHC) is the world's largest particle accelerator with a circumference of 27 km. Superconducting magnets are used to steer two beams of protons around the LHC as they are accelerated to nearly the speed of light. The beams are then brought to collision at various points around the LHC. Located at one of these collision points is the ATLAS detector, one of the two multipurpose detectors at the LHC. The LHC has been colliding protons at a centre-of-mass (COM) energy of 13 TeV since 2015, and ATLAS has been recording data.

The amount of  $pp$  collision data delivered by the LHC is quantified by the *luminosity*. The total number of  $pp$  collisions  $N$  detected over all time  $t$  is related to the cross section for  $pp$  collisions  $\sigma$ , and can be expressed in terms of either the instantaneous luminosity  $L$  or the integrated luminosity  $\mathcal{L}$ :

$$N = \sigma \int L dt = \sigma \mathcal{L} \quad (2.1)$$

$\mathcal{L}$  is the measure of total data collected that is frequently quoted in ATLAS. It has units of  $\text{cm}^{-2}$ , but a more frequently used unit is the inverse barn.  $1 \text{ b} = 10^{-28} \text{ m}^2$ . The total amount of data delivered by the LHC in the 2015-2017 period is  $93 \text{ fb}^{-1}$ . ATLAS has recorded a total of  $86 \text{ fb}^{-1}$ , with  $80 \text{ fb}^{-1}$  that is good for physics analyses.

An overview of the ATLAS detector is shown in Figure 2.4. It is composed of four major subsystems. The innermost system is the inner detector which measures the tracks of charged particles very near to the collision point. It consists of three layers known as the pixel detector, semiconductor tracker, and transition radiation tracker. The innermost pixel detector has the highest resolution granularity in the detector and consists of 80 million pixels. The semiconductor tracker consists of  $60 \text{ m}^2$  of silicon microstrips with densely packed readout channels, and the transition radiation tracker consists of 300,000 wires encased in straw tubes to measure tracks from ionization. The inner detector is encased in a solenoid that exerts a 2 Tesla magnetic field. The magnetic field causes the paths of charged particles to bend. The momentum of the particles can be determined from the curvature of the tracks.

Moving outward from the centre of the detector, the next subsystems are the electromagnetic and hadronic calorimeters. The electromagnetic system is entirely composed of liquid argon calorimetry, while the hadronic system includes the tile calorimeter in the barrel region and liquid argon calorimetry in the end-caps. The calorimeters are dense and designed to stop particles completely so that their energy is deposited entirely inside the detector. The electromagnetic calorimeter is designed to stop particles that interact electromagneti-

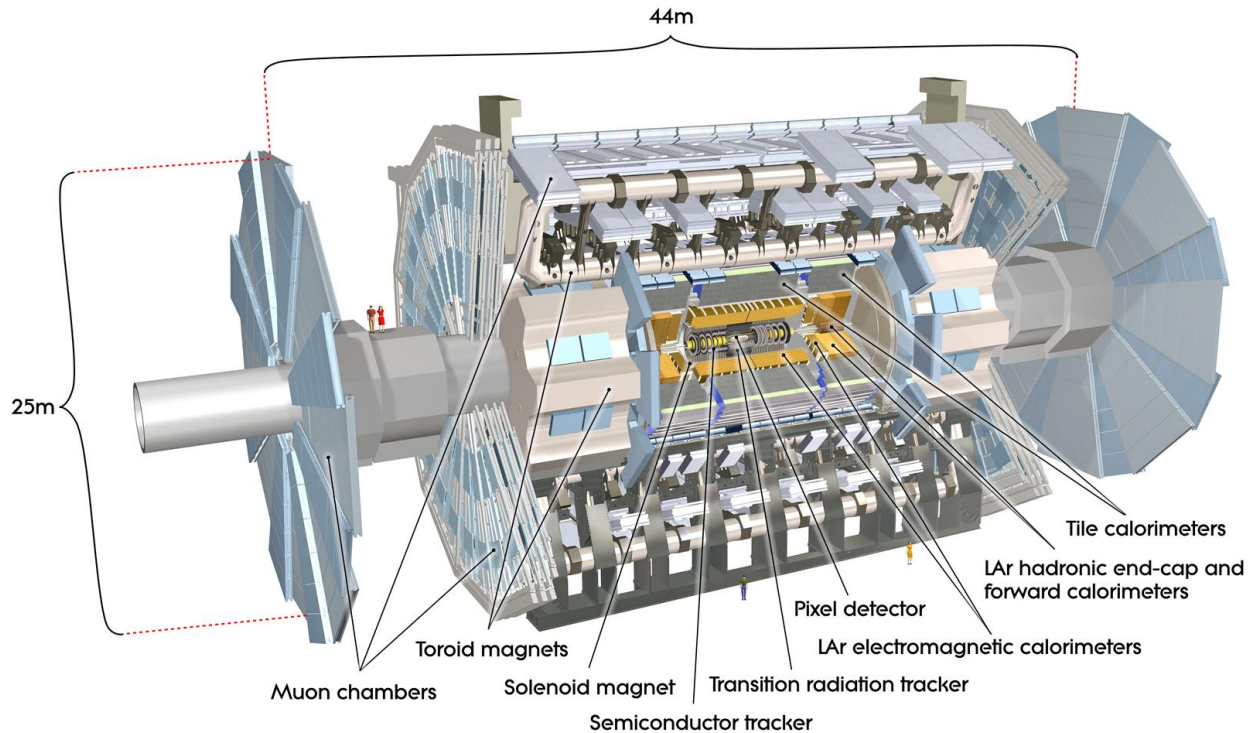


Figure 2.4: A cutaway view of the ATLAS detector with different subsystems labelled. The two humans on the left set the scale of the detector.

cally (electrons and photons) while the hadronic calorimeter is designed to stop hadrons (e.g. protons and neutrons). The liquid argon calorimeter consists of alternating layers of copper absorber material and liquid argon ionization chambers, while the tile calorimeter alternates between layers of steel and plastic scintillators.

The outermost and largest system of the detector is the muon spectrometer. Muons will interact minimally with the detector and so the spectrometer is designed to measure their momenta from tracks. The spectrometer consists of several systems. Monitored drift tubes are used in the barrel and end-caps for measuring track curvature. Resistive plate chambers, cathode strip chambers, and thin gap chambers are used for precision coordinate measurements throughout the spectrometer. The muon spectrometer also contains the ATLAS toroid magnet system.

Events that occur in the detector are recorded by the ATLAS trigger system. Due to the incredibly high rates of collisions inside the detector, it's not feasible to record every event that occurs (and most events are not interesting). The Level 1 trigger is hardware-based and makes decisions based on energy clusters in the calorimeter or coincidences in the muon

spectrometer. If the event passes the Level 1 trigger, then it moves to the High Level Trigger, a more sophisticated software-based algorithm. A single electron trigger in the High Level Trigger may require, for example, that an object meets some electron identification criteria, has some minimum  $p_T$ , and is relatively isolated. The event is recorded to disk if the Level 1 and High Level Trigger selection criteria are satisfied.

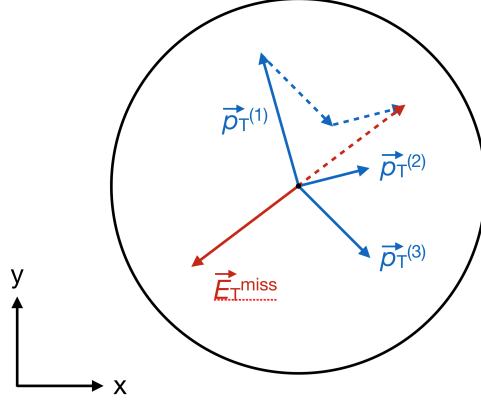


Figure 2.5: Schematic of the missing transverse momentum  $\vec{E}_T^{\text{miss}}$ .

Events that are recorded and deemed to be “good for physics” can be analyzed. The reconstructed objects in the events include electrons, photons, muons, and jets. The  $E_T^{\text{miss}}$  is calculated using the reconstructed objects in the event. Figure 2.5 shows an example of the transverse plane for an event with three measured particles. The  $p_T$  of the reconstructed objects in the event are added together (shown by the red dashed vector). Then the negative is taken to balance the measured  $p_T$  in the event (the solid red vector). This is the  $\vec{E}_T^{\text{miss}}$ . The vector quantity  $\vec{E}_T^{\text{miss}}$  is known as the missing transverse momentum, while its magnitude  $E_T^{\text{miss}}$  is referred to as the missing transverse energy. The formal definition is given by:

$$\vec{E}_T^{\text{miss}} = - \left( \sum \vec{p}_T^{\text{jets}} + \sum \vec{p}_T^{\text{electrons}} + \sum \vec{p}_T^{\text{muons}} + \sum \vec{p}_T^{\text{soft track}} \right) \quad (2.2)$$

The soft track term is formed from leftover tracks that are not used in reconstructed objects. Calorimeter energy clusters can also be used for this term, but tracks are more robust in high pileup environments.

The physics objects used for a given analysis may have to satisfy further, stricter requirements, such as residing in a specific region of the detector. Then those selected objects are used to calculate the kinematic quantities used in the event selection.

# Chapter 3

## The Mono- $Z(\ell\ell)$ Search

This chapter summarizes the work achieved so far. Section 3.1 gives an overview of the analysis, while the following sections discuss specific contributions by the author in more detail. These contributions include estimation of the QCD scale and parton showering systematic uncertainties on the signal acceptance (Section 3.2), estimation of the  $Z$ +jets background using the ABCD method and the  $\gamma$ +jets reweighting technique (Section 3.3), limit setting and reinterpretations of the mono- $Z$  signals (Section 3.4), and development of the analysis software framework (Section 3.5).

### 3.1 Analysis Overview

There are several important aspects of the mono- $Z$  search. The analysis has been repeated fully twice during Run 2, once with the 2015 dataset ( $3.2 \text{ fb}^{-1}$ ) and again with the 2015+2016 dataset ( $36.1 \text{ fb}^{-1}$ ). The next result will not be ready until the full 2015-2018 Run 2 dataset is collected. The techniques discussed in this section are mainly based on the previous results from the 2015+2016 dataset.

One of the the first steps of the analysis is to optimize the event selection for the specific signal being considered in the search. A *signal region* must be chosen using some metric that optimizes the amount of signal compared to background. Background events are caused by SM processes that produce the same signature as the dark matter signal. Ideally such processes should be as suppressed as possible in the signal region. Event selections are optimized using Monte Carlo (MC) simulated events for signal and backgrounds. ATLAS MC are sophisticated and include effects from the detector, such as energy resolution. In general, events are selected in order to isolate a  $e^+e^-$  or  $\mu^+\mu^-$  pair that have an invariant mass close to

the  $Z$  and are recoiling against a sizeable  $\vec{E}_T^{\text{miss}}$ . The most important kinematic variables are identified and calculated using reconstructed objects as measured in the ATLAS detector (approximate in MC). Additional selection requirements are used to reduce background contributions while attempting to preserve signal. Two signal regions are used in the mono- $Z$  analysis, one where  $e^+e^-$  events are selected and the other where  $\mu^+\mu^-$  events are selected. The full list of event selections is given in Appendix A.1.

Another crucial part of the analysis is in-situ background estimation. Once a signal region has been defined, data can then be used to estimate the dominant backgrounds in that region. When possible it is always preferable to use data instead of MC estimations. This is typically done by defining a control region that has a very high purity in background events, and then somehow transferring the estimate into the signal region. The major backgrounds in the analysis are described below with their percent contribution from the 2015+2016 result. They all emulate the signal by producing  $\ell\ell + E_T^{\text{miss}}$ . All backgrounds except for the  $ZZ$  background are estimated from data.

1.  $ZZ \rightarrow \ell\ell\nu\nu$  (56%): Dominant, irreducible background. Estimated entirely with MC.
2.  $WZ \rightarrow \ell\nu\ell\ell$  (27%): Lepton from the  $W$  is not reconstructed.
3.  $Z$ +jets (8%): Jet(s) are mis-measured and produce fake  $E_T^{\text{miss}}$ .
4.  $WW$ ,  $Wt$ ,  $t\bar{t}$ , and  $Z \rightarrow \tau\tau$  (8%): Lepton pair does not come from a  $Z$ .
5.  $W$ +jets ( $< 1\%$ ): A jet is misidentified as a lepton.

The data-driven estimation techniques for each of the backgrounds are complex and are not discussed in detail here. Previous work on the estimation of the  $Z$ +jets background is discussed in Section 3.3.

There are several sources of systematic errors that must be considered in any ATLAS analysis. Experimental systematics come from detector effects, such as the uncertainty in identifying an electron, energy uncertainties due to resolution effects, etc. These systematic errors are typically estimated using dedicated analyses and are applied to MC samples. Data-driven background estimates will have systematic errors associated with the specific estimation technique. These types of systematics are often the dominant source of systematic uncertainties. Finally, there are theoretical systematics associated with the simulated dark matter signal, including errors from QCD, PDF, and parton showering effects. These will be discussed in more detail in the following section.

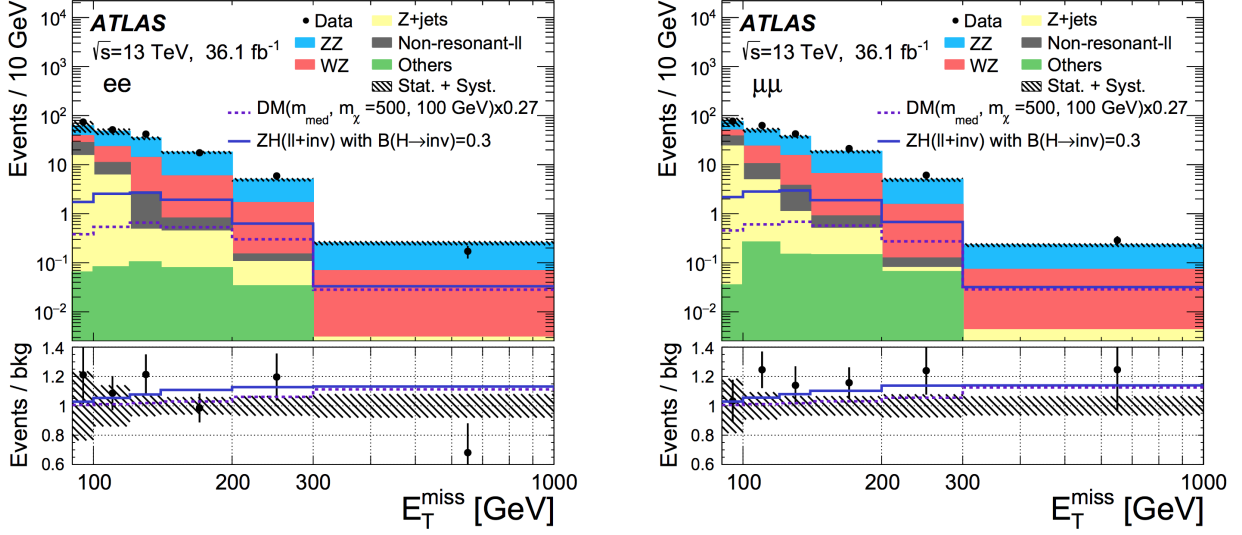


Figure 3.1:  $E_T^{\text{miss}}$  distributions in the  $ee$  (left) and  $\mu\mu$  (right) signal regions with  $36.1 \text{ fb}^{-1}$  [5].

After defining a signal region, estimating backgrounds in that signal region, and accounting for the systematic uncertainties of the analysis, the signal region is *unblinded* and the agreement between observed data and expected background estimates is quantified. In the mono- $Z$  analysis the  $E_T^{\text{miss}}$  is the distribution of interest, where a dark matter signal could manifest. The signal region  $E_T^{\text{miss}}$  distributions from the 2015+2016 analysis are shown in Figure 3.1. If an excess in data is found then there is potential for a discovery. However, as in past iterations of the analysis, if no excess is seen then limits can be set on the dark matter model being studied. This is discussed in detail in the final section of this chapter.

## 3.2 Truth Studies

Truth studies are often useful when we want to ignore the effects of the ATLAS detector. *Reconstructed* MC samples include simulation of the detector, whereas *truth-level* MC samples come directly from the MC generator, typically MADGRAPH [9]. Studying these samples allow us to study theoretical effects on the signal. In addition, such samples can be produced quickly and locally, whereas reconstructed samples must undergo ATLAS reconstruction which can be computationally intensive.

A framework has been adapted, called MonoZTruthUVic, for applying truth-equivalent analysis cuts to truth samples. This allows for the analysis to be reproduced at the truth-level. This is useful for several reasons and allows us to estimate how many signal events are

theoretically predicted to be in the signal region.

An important study that must be performed at the truth-level is the estimation of theoretical uncertainties on the signal *acceptance*, the fraction of signal events that end up in the signal region. There are potentially significant sources of systematic uncertainties from theory that must be considered. It should be noted that systematics from uncertainties in the parton distribution function (PDF) are also evaluated in the analysis but are not discussed in detail here.

The signal yield and acceptance depend on two scales from quantum chromodynamics (QCD) known as the renormalization and factorization scales,  $\mu_r$  and  $\mu_f$ . Both scales are arbitrary and arise from finite order perturbation theory.  $\mu_r$  is related to the renormalization of ultraviolet divergences, and  $\mu_f$  qualitatively corresponds to the resolution at which the proton is being probed. From the QCD factorization ansatz [10], the cross section for a hard process resulting from the collision of two protons with momenta  $p_1$  and  $p_2$  can be written in terms of  $\mu_f$  and  $\mu_r$  as

$$\sigma = \int dx_1 dx_2 f_1(x_1, \mu_f^2) f_2(x_2, \mu_f^2) \hat{\sigma}(x_1 p_1, x_2 p_2, \alpha_s(\mu_r), Q^2, \mu_r^2, \mu_f^2), \quad (3.1)$$

where partons 1 and 2 have PDFs  $f_1$  and  $f_2$  and momentum fractions of the protons  $x_1$  and  $x_2$  respectively.  $Q$  is the scale of the hard scatter process determined by the cross section  $\hat{\sigma}$ , and  $\alpha_s$  is the strong coupling constant. The main assumption of this formula is that at high energies the timescale of the collision is much shorter than the parton-parton interactions within a single proton. Hence, partons 1 and 2 can be treated as free with definite momentum fractions  $x_1$  and  $x_2$ . The total cross section is then calculated from the probability (modelled by the PDFs) for two partons with given momentum fractions to interact.

$\hat{\sigma}$  is calculated to some finite order  $n$  in  $\alpha_s$  according to  $\hat{\sigma}^{(n)} = \alpha_s \hat{\sigma}^{(0)} + \alpha_s^2 \hat{\sigma}^{(1)} + \dots + \alpha_s^n \hat{\sigma}^{(n)} + \mathcal{O}(\alpha_s^{n+1})$ . The uncertainties on  $\mu_f$  and  $\mu_r$  provide an estimate on  $\mathcal{O}(\alpha_s^{n+1})$ . By simulating dark matter MC with different values for  $\mu_f$  and  $\mu_r$  and then applying truth-level analysis cuts, the systematic error on the acceptance due to the choice of scales can be quantified. The convention is to generate two modified samples with  $\mu_r = \mu_f$ , where the scales are doubled in one sample and halved in the other. Then the signal acceptance for both modified samples is calculated and compared to the nominal acceptance. The largest change is taken as the systematic error. This systematic has been observed to be independent of  $m_\chi$ , so the errors are evaluated as a function of  $m_{\text{med}}$ . An example of the errors previously used for axial-vector signals is illustrated in Figure 3.2. These errors are on the order of 1-2% for most masses.

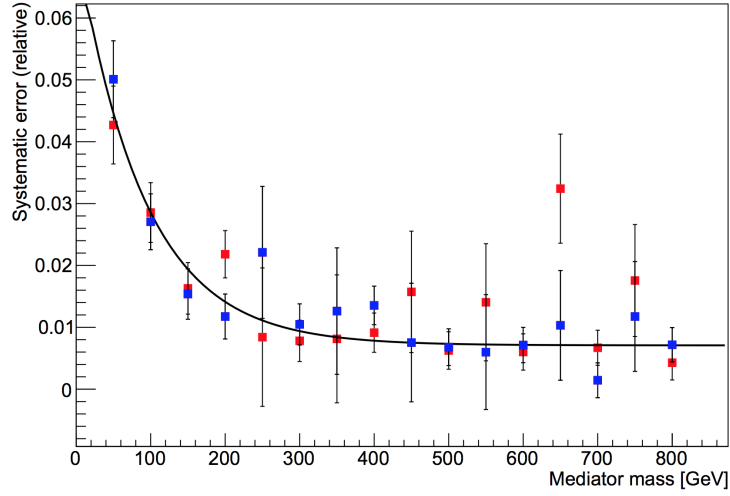


Figure 3.2: QCD scale uncertainties on the signal acceptance as a function of mediator mass for axial-vector signals. Produced by the author. Red and blue points correspond to errors obtained from the  $ee$  and  $\mu\mu$  signal regions respectively.

The other source of theoretical uncertainty on the signal acceptance comes from parton showering effects. In the MC samples used by ATLAS, after the hard scatter is simulated it is run through a showering simulator called PYTHIA [11]. PYTHIA adds in several physical effects such as the underlying event, initial and final state radiation of extra jets, and multiple parton interactions. These are complicated processes governed by QCD and a number of parameters in PYTHIA can be set. To simplify this, ATLAS has a standardized PYTHIA *tune*, i.e. a set of parameters that serves as the default to be used in MC showering. The signal acceptance depends on the choice of this tune. The uncertainty is evaluated using a prescription whereby ten variations are used to account for each general effect. As for the QCD scale uncertainties, modified MC samples are produced according to each variation, and the difference in the signal acceptance is evaluated compared to the nominal showering. These systematics are typically on the order of 5%.

### 3.3 Estimation of the $Z$ +jets Background

#### 3.3.1 ABCD Method

One data-driven technique for estimating the  $Z$ +jets background is the ABCD method. This was the primary estimation method used for the 2015 dataset. A schematic of the method is shown in Figure 3.3. Four regions are defined using two of the kinematic variables from the



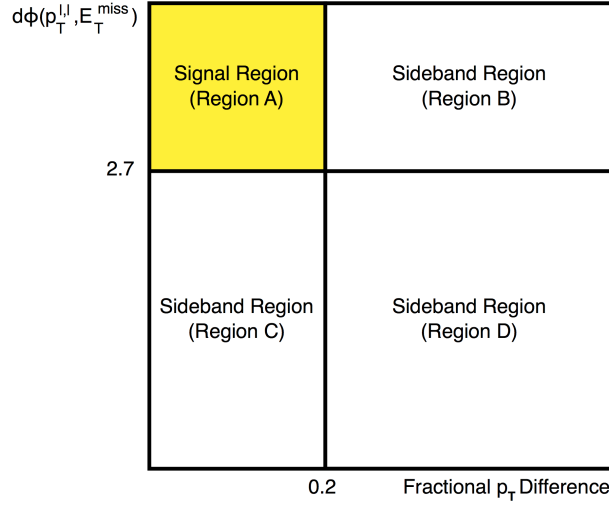


Figure 3.3: Scheme of the ABCD method used with the 2015 dataset.

event selection. This pair of variables is chosen to optimize event statistics in the sideband regions (B, C, and D) and to minimize the correlation between them. Region A is the signal region, the target region that we are trying to estimate the background in. The number of background events in the sidebands are used to estimate the number of background events in A using the assumption that  $N_A/N_C = N_B/N_D$ . This is true if there is no correlation between the two variables. Then the number of  $Z$ +jets events in A is given by:

$$N_A^{\text{est}} = N_C^{\text{obs,corr}} \times \frac{N_B^{\text{obs,corr}}}{N_D^{\text{obs,corr}}} \quad (3.2)$$

$N_B$ ,  $N_C$ , and  $N_D$  are the observed number of events in each sideband control region with non- $Z$ +jets events subtracted (using MC).

The main challenges for this method come from having some correlations between the two variables and having enough statistics in data in all of the sidebands. The validity of this technique is evaluated by looking at the agreement between the three ratios  $N_A/N_C$  (MC),  $N_B/N_D$  (MC), and  $N_B/N_D$  (data). If the method works perfectly then these ratios will agree. In addition, the agreement of these ratios should agree as the other event selections are applied. However, correlations cause deviations in the agreement, and low statistics in one or more of the sidebands can lead to large errors on the ratios after all selections are applied. And, if the ratios change with other selections, this suggests more complicated correlations with other variables that enhance the correlation between the two variables used for the method. These effects are all taken into account with systematic errors that are evaluated to be about  $\pm 70\%$  on the  $Z$ +jets estimate. These errors turned out to be

dominant uncertainties in the analysis on the 2015 dataset.

### 3.3.2 $\gamma$ +jets Technique

The  $Z$ +jets estimation had to be modified for the 2015+2016 dataset. The event selection was reoptimized with the introduction of new variables, and correlations had a more pronounced effect in the ABCD method. Because of this, a second technique was developed alongside a modified ABCD method. The technique is known as the  $\gamma$ +jets reweighting method. The theory is described in [12] and the application has been adapted from an ATLAS SUSY search [13].

The  $\gamma$ +jets method uses events with a photon and jets to estimate the fake  $E_T^{\text{miss}}$  in  $Z$ +jets events.  $\gamma$ +jets event topologies are similar to  $Z$ +jets events as they both consist of a well-measured  $Z$  or photon recoiling against jets, and the  $E_T^{\text{miss}}$  arises from jet mis-measurements. However there are some kinematic differences that need to be accounted for. This is done by reweighting the  $\gamma$ +jets MC events to transport them to  $Z$ +jets MC events. Typically the  $p_T$  distribution of the photon is scaled to match the  $p_T$  distribution of the  $Z$  (i.e. the  $p_T$  of the two leptons). The multiplicative factor needed to scale each  $p_T$  bin is used as an event weight for the  $\gamma$ +jets events:

$$w(p_T^\gamma) = \frac{N_{Z+\text{jets}}(p_T^{\ell\ell})}{N_{\gamma+\text{jets}}(p_T^\gamma)} \quad (3.3)$$

After the reweighting the  $E_T^{\text{miss}}$  distribution for the  $\gamma$ +jets events improves to match the  $Z$ +jets events (most obviously the tail increases at high  $E_T^{\text{miss}}$ ). The reweighting is applied fairly early in the event selection and then subsequent selections are applied; the agreement between  $\gamma$ +jets and  $Z$ +jets events is monitored down to the signal region. Once reliable agreement is seen, then the method can be performed using data instead of MC.

In the mono- $Z$  analysis,  $p_T$  reweighting was not sufficient to have good agreement between  $\gamma$ +jets and  $Z$ +jets events. Two approaches were taken in an attempt to rectify the remaining differences. The first is a photon smearing method as used in [13]. This is done by looking at the component of the  $E_T^{\text{miss}}$  along the  $Z$ /photon direction,  $E_{T,\parallel}^{\text{miss}}$ . The idea is that any difference in  $E_{T,\parallel}^{\text{miss}}$  between  $Z$ +jets and  $\gamma$ +jets events comes from lepton mis-measurements in the  $Z$ +jets events, leading to a worse  $Z$  resolution compared to the photon. Hence the photon  $p_T$  and  $E_{T,\parallel}^{\text{miss}}$  can be smeared to match the  $Z$  resolution. This procedure was carried out in the mono- $Z$  analysis but minimal improvements were seen because the photon and  $Z$  were observed to have very similar resolutions. Therefore a second reweighting scheme was

adapted to improve the agreement in the  $E_T^{\text{miss}}$  distributions. Instead of only reweighting by  $p_T$ , a secondary reweighting is applied using another variable. Several variables were investigated; in the end  $E_T^{\text{miss}}/H_T$  gave the best results ( $H_T$  = scalar sum of lepton  $p_T$  and jet  $p_T$ ). In addition, the reweighting could be applied using 2D weights or with two 1D (2x1D) weights. The 2D reweightings that were investigated gave the best  $E_T^{\text{miss}}$  agreement, but the weights were unreliable due to limited statistics (e.g. weights in  $p_T$  and  $E_T^{\text{miss}}/H_T$  bins). 2x1D reweighting schemes were also studied. Here an added complication is that the two variables that are reweighted are treated as uncorrelated, whereas for 2D reweighting the correlation is accounted for automatically. So in a 2x1D scheme, when reweighting the second variable, if the previously reweighted  $p_T$  distribution does not change, then the variables can be treated as uncorrelated. This was seen in  $p_T$  and  $E_T^{\text{miss}}/H_T$ . Also the weights with 2x1D schemes were observed to be far more reliable because of the higher statistics use in the weight calculation. This was further tested by splitting the  $\gamma$ +jets MC into two statistically independent halves; one half was used to obtain the weights and the other half had them applied. The agreement between both reweighted halves of the  $\gamma$ +jets sample was excellent.

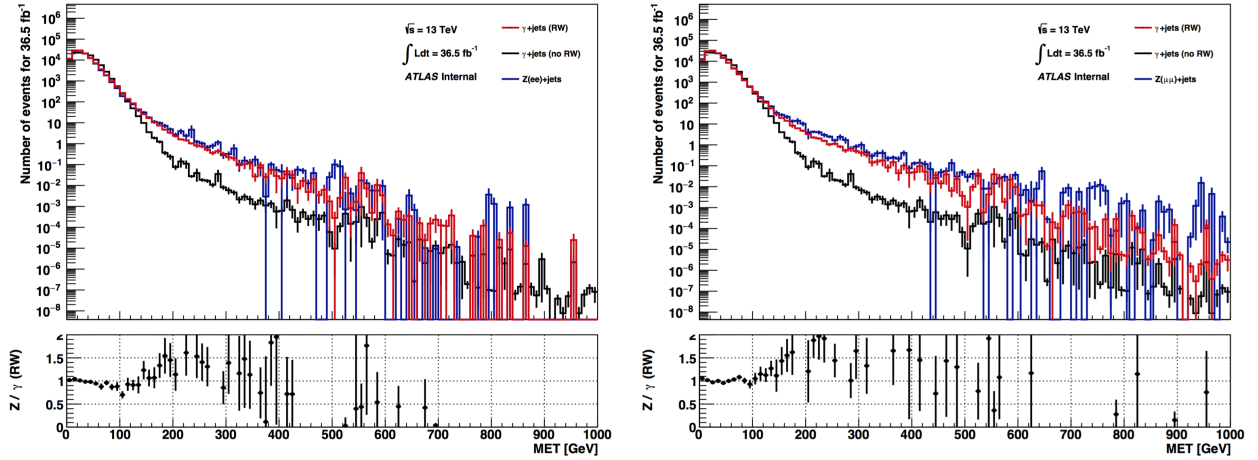


Figure 3.4:  $E_T^{\text{miss}}$  distributions for  $\gamma$ +jets events (red) and  $Z$ +jets events (black without reweighting, blue with reweighting). Produced by the author.

Due to time constraints in the analysis for the 2015+2016 dataset, the development of this technique is still under development and has yet to be tested on data. In the end a 2x1D reweighting scheme using  $p_T$  and  $E_T^{\text{miss}}/H_T$  gave the best results in MC. Figure 3.4 shows the  $E_T^{\text{miss}}$  distributions for  $Z$ +jets and reweighted  $\gamma$ +jets events (at an early selection step). From  $Z$ +jets MC, the predicted yield in the  $ee$  and  $\mu\mu$  signal regions is approximately  $0.45 \pm 0.90$  events. The best observed reweighted  $\gamma$ +jets prediction is  $2.0 \pm 0.1$ . The results nearly agree within statistical errors, but differences are still observed in the  $E_T^{\text{miss}}$  tail. Since this is the

region of interest in the mono- $Z$  search, care must be taken to study these differences and quantify the systematic errors from the reweighting technique. The next steps to developing and improving the  $\gamma$ +jets technique are discussed in the next chapter.

### 3.4 Dark Matter Limit Setting

In the case that no excess is observed in data, upper limits are set on the signal strength for each of the dark matter models. These are then translated into limits on the masses of the dark matter particles,  $m_\chi$  and  $m_{\text{med}}$ . Hypothesis tests are performed using the HISTFITTER [14] framework. The signal region  $E_T^{\text{miss}}$  distributions are inputted to HISTFITTER for data, expected signal and backgrounds, and all systematic uncertainty variations. HISTFITTER is then used to calculate upper limits on the amount of signal using the  $\text{CL}_s$  method [15], a standard in the ATLAS experiment.

The statistical analysis of the data uses a binned likelihood function constructed as:

$$L(\mu, \boldsymbol{\theta}) = \prod_{i=1}^N \frac{(\mu s_i + b_i)^{n_i}}{n_i!} e^{-(\mu s_i + b_i)} \times \prod_{j=1}^M G(\theta_j^0, \theta_j) \quad (3.4)$$

The first factor is the product of Poisson probabilities to observe  $n_i$  events for each signal region bin  $i$  that has  $\mu s_i + b_i$  expected events.  $s_i$  and  $b_i$  are the predicted signal and background yields in each bin, and  $\mu$  is the signal strength parameter (also called the *parameter of interest*).  $\mu = 0$  is the background-only hypothesis, and  $\mu = 1$  is the signal+background hypothesis. The dependence of the signal and background predictions on the systematic uncertainties is described by a set of nuisance parameters  $\vec{\theta}$  ( $= \boldsymbol{\theta}$ ), which are each parametrized by a Gaussian. The second factor in Equation 3.4 is a product of these terms over all systematics, where  $\theta_j^0$  is the measured central value around which  $\theta_j$  varies. In HISTFITTER the  $G$ 's are parametrized so that each  $\theta_j^0$  is fixed to 0 with standard deviation = 1.

The nominal fit result is obtained by maximizing the likelihood function with respect to all parameters. This is referred to as the maximum likelihood,  $L(\hat{\mu}, \hat{\boldsymbol{\theta}})$ , where  $\hat{\mu}$  and  $\hat{\boldsymbol{\theta}}$  are the parameters that maximize the likelihood. The *test statistic*,  $\tilde{q}_\mu$ , is then constructed based on profile likelihood ratios as:

$$\tilde{q}_\mu = \begin{cases} -2 \ln \frac{L(\mu, \hat{\boldsymbol{\theta}}(\mu))}{L(0, \hat{\boldsymbol{\theta}}(0))} & \hat{\mu} < 0 \\ -2 \ln \frac{L(\mu, \hat{\boldsymbol{\theta}}(\mu))}{L(\hat{\mu}, \hat{\boldsymbol{\theta}})} & 0 \leq \hat{\mu} \leq \mu \\ 0 & \hat{\mu} > \mu \end{cases} \quad (3.5)$$

$\hat{\boldsymbol{\theta}}$  are the nuisance parameter values that maximize the likelihood for a fixed  $\mu$ . Larger values of  $\tilde{q}_\mu$  are interpreted as greater incompatibility between measurement and the  $\mu$  hypothesis. The corresponding p-value,  $p_\mu$ , is then defined as:

$$p_\mu = \int_{\tilde{q}_{\mu, \text{obs}}}^{\infty} f(\tilde{q}_\mu | \mu) d\tilde{q}_\mu \quad (3.6)$$

Here  $f(\tilde{q}_\mu | \mu)$  is the probability density function of  $\tilde{q}_\mu$  assuming the  $\mu$  hypothesis, and  $\tilde{q}_{\mu, \text{obs}}$  is the value of  $\tilde{q}_\mu$  computed for the observed data. Asymptotic formulae [15] are used to calculate the closed form of  $f(\tilde{q}_\mu | \mu)$ .  $p_\mu$  can also be written as:

$$p_\mu \equiv p_{s+b} = P(\tilde{q}_\mu \geq \tilde{q}_{\mu, \text{obs}} | s+b) \quad (3.7)$$

Hence it is the probability to observe a test statistic greater than or equal to the observed value, given that the  $s+b$  ( $\mu = 1$ ) hypothesis is true. Performing exclusion tests with  $p_{s+b}$  is known as the  $\text{CL}_{s+b}$  method. This analysis uses the  $\text{CL}_s$  method, where the p-value, or the “ $\text{CL}_s$  value,” is defined as:

$$\text{CL}_s \equiv \frac{p_{s+b}}{1 - p_b}, \quad (3.8)$$

where

$$p_b = P(\tilde{q}_\mu \leq \tilde{q}_{\mu, \text{obs}} | b). \quad (3.9)$$

Using the  $\text{CL}_s$  method,  $\mu$  values that give  $\text{CL}_s < 0.05$  are excluded at the 95% confidence level (CL). These upper limits on  $\mu$  are then extracted from HISTFITTER, and dark matter mass exclusion limits are produced using the MonoZLimitsUVic framework that was written for this purpose.

Figure 3.5 shows the exclusion limits from the 2015+2016 dataset on  $m_\chi$  vs  $m_{\text{med}}$  for axial-vector and vector mediators from the LO simplified models. The mass region inside the contour is excluded at the 95% CL. The relic density line indicates where the particles and interactions of the model are by themselves sufficient for explaining the observed DM

abundance in the universe.

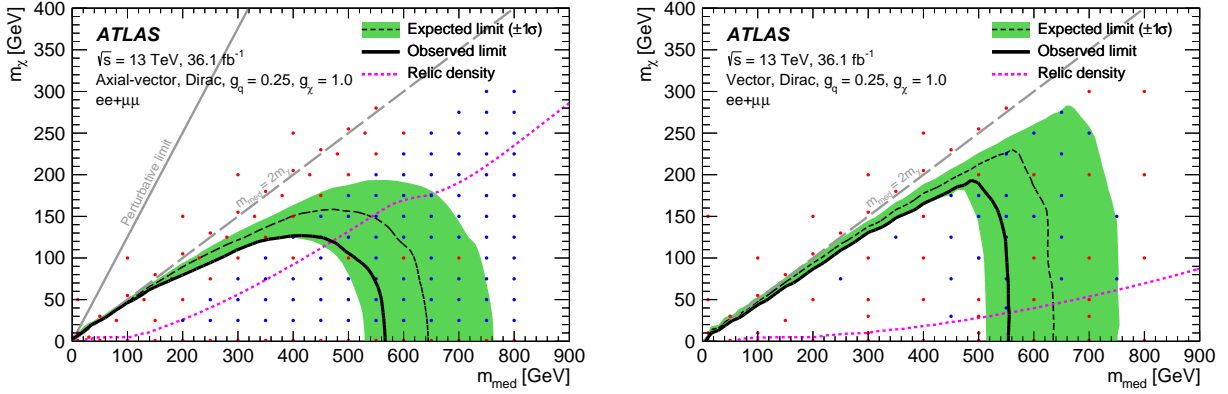


Figure 3.5: Axial-vector (left) and vector (right) exclusion limits on  $m_\chi$  vs  $m_{\text{med}}$  with  $36.1 \text{ fb}^{-1}$  [5]. Produced by the author. The dashed black line is the expected limit with  $\pm 1\sigma$  error bands in green. The solid black line is the observed limit. The relic density calculation for the assumed dark matter model is illustrated by the magenta line. The dashed grey line is the on-shell line where  $m_{\text{med}} = 2m_\chi$ .

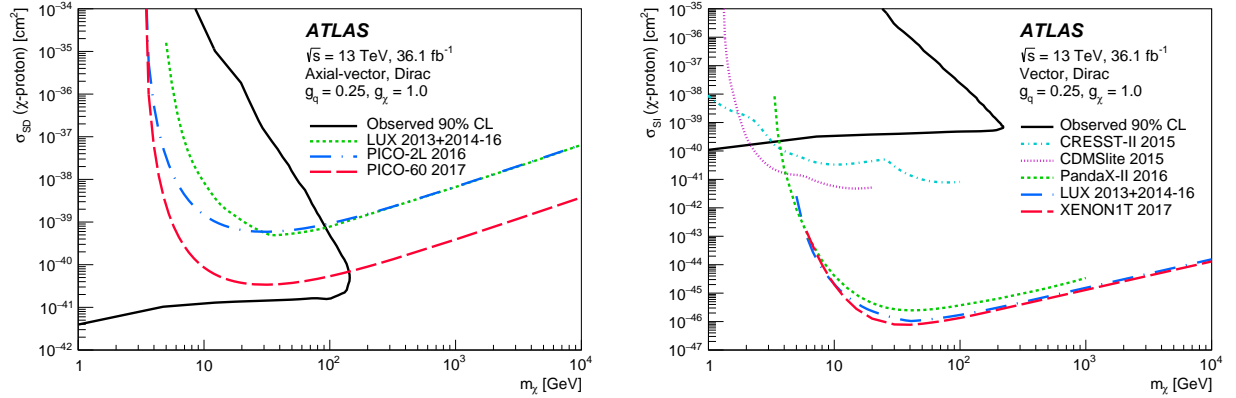


Figure 3.6: Spin-dependent (left) and spin-independent (right) exclusion limits on the DM-proton scattering cross section vs  $m_{\text{med}}$  with  $36.1 \text{ fb}^{-1}$  [5]. Produced by the author. The solid black line indicates the 90% CL ATLAS result, and the coloured lines indicate direct detection measurements.

The 2D mass limits have also been recast into limits on the DM-proton scattering cross section for comparison with direct detection experiments. The procedure for doing so is given in [3]. Figure 3.6 shows the recast mono- $Z$  limits for the spin-dependent and spin-independent scattering cross sections vs  $m_{\text{med}}$ . The cross section is spin-dependent if the

isotope used in the direct detection experiment has an unpaired proton or neutron. The limits shown are at the 90% CL in accordance with the standard used by direct detection experiments. The coloured lines overlaid are limits set by direct detection experiments. The region enclosed by the ATLAS result, and above each coloured line, is excluded at the 90% CL.

Exclusion limits on the 2HDM+PS model have also been set with the 2015+2016 dataset. These are shown in Figure 3.7. Limits are set on  $m_H$  vs  $m_a$  as well as  $\tan\beta$  vs  $m_a$ . The region inside the contour is excluded.

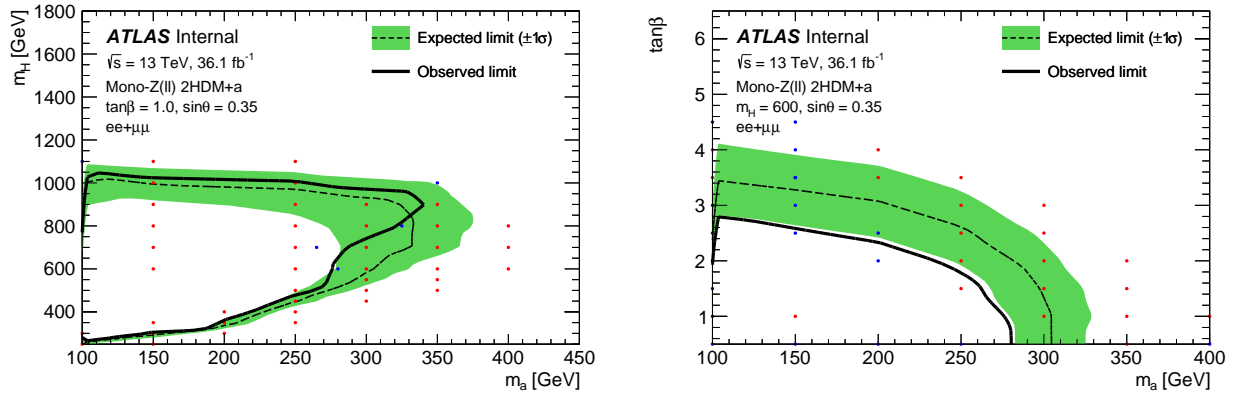


Figure 3.7:  $m_H$  vs  $m_a$  (left) and  $\tan\beta$  vs  $m_a$  (right) exclusion limits with  $36.1 \text{ fb}^{-1}$  (preliminary internal result). Produced by the author. The dashed black line is the expected limit with  $\pm 1\sigma$  error bands in green. The solid black line is the observed limit.

In the mass limits above, the red points indicate the masses at which there are reconstructed signal samples. The blue points indicate *emulated* points. Mass point emulation is performed to create a finer grid of signal samples without using reconstructed samples. The exclusion contour may look jagged in areas with a coarse grid of signal points. By adding in emulated points, the contour can be made smoother and more physical without going through the tedious process of requesting additional reconstructed MC samples. The method discussed here has been used for the LO simplified models with  $36.1 \text{ fb}^{-1}$ ; emulation for the 2HDM+PS model is more complicated and is not discussed here.

The validity of emulating signal samples relies on the assumption that the kinematics (i.e. the  $E_T^{\text{miss}}$  distributions) of the signal does not depend on  $m_\chi$  in the on-shell region (where  $m_{\text{med}} > 2m_\chi$ ). If this is true, then the  $E_T^{\text{miss}}$  distribution for a reconstructed sample at a given  $m_{\text{med}}$  can be used as the  $E_T^{\text{miss}}$  distribution for other signal samples with the same  $m_{\text{med}}$ . However, the  $E_T^{\text{miss}}$  distribution for the emulated sample must be scaled by the ratio

of cross sections  $\sigma_{\text{reco}}/\sigma_{\text{emul}}$ . So, as long as the grid of reconstructed points is fine along  $m_{\text{med}}$ , additional points with different  $m_\chi$  can be emulated just by using the cross sections.

For the axial-vector model, studies on the signal acceptance were performed and verified that the signal acceptance does not depend on  $m_\chi$  when  $m_{\text{med}}$  is constant. For the vector model, an additional complication was that we had a fairly coarse granularity of reconstructed points along  $m_{\text{med}}$ . Because of this, we exploited the similar kinematics between the axial-vector and vector signals and performed emulation from axial-vector to vector samples. Emulation for both models has become customary in the mono- $Z$  analysis and will continue to be used moving forward towards the full dataset analysis.

### 3.5 Analysis Software

The MonoZUVic software package is the core of the analysis and has been developed by the UVic group for the past few years. Throughout the evolution of the analysis, contributions have been made towards writing and maintaining the software. The software must be capable of running the entire analysis, including object (electron, muon, jet) calibrations/corrections/selections, removal of overlaps between objects, applying event selections, calculating event weights and kinematic variables, evaluating experimental systematics, and in the end producing trees/histograms for data and MC. Items such as calibration recommendations and data formats change frequently, and diligent efforts are made to keep the code updated. The software is also cross checked with other groups running the analysis to ensure updated calibrations, prevent errors, etc. The MonoZTruthUVic and MonoZLimit-sUVic packages, mentioned briefly above, were developed by the author to perform truth-level studies and produce exclusion limits. These packages are also maintained alongside MonoZUVic. Contributions have also been made to design overhauls in the framework as the analysis has evolved and improved.



## Chapter 4

# Analysis with the Full Run 2 Dataset

### 4.1 Event Selection Optimization

For the full Run 2 analysis the event selection for the signal region will need to be reoptimized. In practice this is done by defining multiple potential signal regions with each cut varied in intervals (e.g.  $E_T^{\text{miss}} > 80, 85, 90, 95, 100, \dots$  GeV). Then in each region the signal significance  $Z$  is calculated. The formula used in the past iterations of the analysis is given by [16]:

$$Z = \sqrt{2 \left( (s + b) \ln \left( 1 + \frac{s}{b} \right) - s \right)} \quad (4.1)$$

$s$  and  $b$  are the expected number of signal and background events in MC, and  $s + b$  follows a Poisson distribution. If  $s \ll b$  then the formula reduces to  $Z = s/\sqrt{b}$ . The main caveat with this formula however is that the uncertainty on  $b$  is considered to be negligible. If one takes the uncertainty on  $b$  to be  $\sigma_b$ , then the formula becomes [16]:

$$Z = \sqrt{2 \left( (s + b) \ln \left( \frac{(s + b)(b + \sigma_b^2)}{b^2 + (s + b)\sigma_b^2} \right) - \frac{b^2}{\sigma_b^2} \ln \left( 1 + \frac{\sigma_b^2 s}{b(b + \sigma_b^2)} \right) \right)} \quad (4.2)$$

This formula reduces to  $Z = s/\sqrt{b + \sigma_b^2}$  for  $s \ll b$  and  $\sigma_b^2 \ll b$ . Using this formula would be an improvement compared to using Equation 4.1. The significance is estimated from MC, so the uncertainties  $\sigma_b$  could be either (a) the experimental systematics as applied to the MC, or possibly (b) approximated from the much larger data-driven uncertainties on the background estimates from the 2015+2016 dataset. These uncertainties were calculated in a specific signal region, but their approximate magnitudes could be useful for estimating a more correct significance.

A reoptimization of the signal region is also motivated by newly available  $E_T^{\text{miss}}$ -related quantities that could improve the mono- $Z$  analysis. For example, two  $E_T^{\text{miss}}$  working points are now available. In the new “tight”  $E_T^{\text{miss}}$  definition, jets in the forward region of the detector must have  $p_T > 30$  GeV to reduce contributions from pileup. The “loose” definition (used previously in this analysis) includes all jets with  $p_T > 20$  GeV except for forward jets with  $p_T < 60$  GeV that fail an additional minimum jet vertex tagger requirement, a multivariate criteria that identifies pileup jets from tracks. The tight definition is now recommended because the  $E_T^{\text{miss}}$  resolution is improved. Both definitions will be studied to validate the improvement in switching to the tight definition.

There is also now the option to use particle-flow  $E_T^{\text{miss}}$ , which is calculated using particle-flow jets. The particle-flow algorithm [17] uses information from both the tracker and the calorimeter to determine the energy of a jet. Traditional jets are constructed only using energy deposits in the calorimeter. The tracker has better energy resolution than the calorimeter (for particles with low momentum), better angular resolution, and can better detect soft charged particles that may not meet the noise threshold of the calorimeter. Particle-flow jets may be a better option for calculating a more reliable  $E_T^{\text{miss}}$ , especially in higher pileup conditions. Particle-flow  $E_T^{\text{miss}}$  will need to be studied and compared with the traditional  $E_T^{\text{miss}}$  to determine which is better suited for the analysis.

Another new variable is the  $E_T^{\text{miss}}$  significance  $\mathcal{S}$  [18]. It is defined using a log-likelihood ratio and quantifies how likely it is that the reconstructed  $\vec{E}_T^{\text{miss}}$  is consistent with genuine  $\vec{E}_T^{\text{miss}} \neq 0$  (i.e. that there are real invisible particles in the event, as opposed to a non-zero  $\vec{E}_T^{\text{miss}}$  from particle measurement resolution and efficiency effects). It is defined as

$$\mathcal{S}^2 = 2 \ln \left( \frac{\mathcal{L}(\vec{E}_T^{\text{miss}} | \vec{p}_T^{\text{inv}} \neq 0)}{\mathcal{L}(\vec{E}_T^{\text{miss}} | \vec{p}_T^{\text{inv}} = 0)} \right), \quad (4.3)$$

where  $\vec{p}_T^{\text{inv}} = -\vec{E}_T^{\text{miss}}$ . A large  $\mathcal{S}$  indicates that the  $\vec{E}_T^{\text{miss}}$  is not well explained by resolution smearing effects, and real invisible particles are likely to be in the event. This discriminant is more powerful in rejecting events with fake  $E_T^{\text{miss}}$  from mis-measured objects (compared to more traditional variables such as  $E_T^{\text{miss}}/H_T$ ) because it includes the uncertainties of the reconstructed objects and track-based soft term that enter the  $E_T^{\text{miss}}$  calculation. Hence this is a promising variable to help reduce the  $Z$ +jets background, arguably the most difficult background to estimate in this analysis.

Finally, an added complication in the future event selection optimization of the analysis is the potential for multiple signal regions. As we study more varieties of dark matter models, the cuts that optimize the significance for different signals may differ. If the significance for

different signals varies greatly with different cuts, it may be optimal to have more than one signal region. However, this adds additional challenges to the analysis, such as having to estimate backgrounds in multiple regions; if a background is difficult to estimate (e.g. large correlations when estimating  $Z$ +jets with the ABCD method), this can increase the amount of time needed to validate the technique and obtain a reasonable data-driven estimate. Since the analysis has limited manpower, it may be decided to have a slightly sub-optimal signal region and sacrifice some significance. These types of decisions will have to be discussed in the group moving forward.

## 4.2 Development of the $\gamma$ +jets Technique

The  $\gamma$ +jets method for estimating the  $Z$ +jets background is under development. For the 2015+2016 dataset, a heavily modified ABCD method was used for the  $Z$ +jets data-driven estimate. The systematic errors on the estimate were large, on the order of 50-100%. It would be desirable to have a more reliable estimate for this background from the  $\gamma$ +jets method for the full Run 2 result.

As discussed in Section 3.3.2, for the 2015+2016 dataset acceptable agreement was obtained between MC  $\gamma$ +jets and  $Z$ +jets events in the signal region, with the estimates nearly agreeing within statistical errors. The method used a 2x1D reweighting scheme with the boson  $p_T$  and the  $E_T^{\text{miss}}/H_T$ . After the reoptimization of the event selection, this scheme may change. For example, with the introduction of the  $E_T^{\text{miss}}$  significance described in the previous section, it may be better to redo the  $\gamma$ +jets estimate with  $p_T$  and  $\mathcal{S}$ , that is if  $\mathcal{S}$  is chosen to be included in the event selection. Depending on the selections chosen, it could be worth reinvestigating a few of the more promising pairs of variables with which to perform the reweighting. In addition, the improved statistics of the Run 2 dataset may provide opportunity for more reliable 2D weights, but this will need to be assessed. It may also be worthwhile to investigate the effects of the reweighting before/after certain cuts. For example, the largest disagreement between  $\gamma$ +jets and  $Z$ +jets events in the cutflow was seen at the  $E_T^{\text{miss}}$  (and  $E_T^{\text{miss}}/H_T$ ) cut. It could be that reweighting the events after the  $E_T^{\text{miss}}$  requirement may help to improve the agreement.

Once acceptable agreement is seen in  $\gamma$ +jets and  $Z$ +jets events, the next step would be to apply the method to data. A few methods for doing this have been discussed. For example, should the weights be obtained from data or MC? This may depend on which has more reliable statistics. The validation of the weights must also be tested, for example by applying weights obtained in MC to data and then looking at the agreement with the

reweighted MC. Differences seen in the agreement must then be quantified as systematic errors in the technique.

There is also the technical side of implementing the  $\gamma$ +jets technique in the MonoZUVic software. This was done previously for the 2015+2016 dataset, but since then the code has undergone a significant redesign, and the  $\gamma$ +jets estimate will need to be reimplemented.

### 4.3 Signal Models

More dark matter models will be studied in the mono- $Z$  analysis with the full Run 2 dataset. As recommended by the LHC DM Working Group,  $s$ -channel simplified models with spin-0 mediators will continue to be the benchmark model used in the analysis; however signals will be simulated at next-to-leading order (NLO) in QCD rather than LO, as higher-order QCD corrections have been shown to have a significant impact on the production rate and kinematic distributions of these models [19]. In addition, these models allow for mediator couplings to leptons. In total there are four NLO benchmark scenarios recommended [20] with the following couplings:

Model	Mediator	$g_q$	$g_\ell$	$g_\chi$
A1	axial-vector	0.25	0.0	1.0
A2	axial-vector	0.1	0.1	1.0
V1	vector	0.25	0.0	1.0
V2	vector	0.1	0.01	1.0

Table 4.1: Benchmarks for NLO  $s$ -channel simplified models in Run 2.

Recent work [21] has shown that it is possible to rescale from A1 to A2 and V1 to V2 using the ratio of cross sections. We are currently working on sample requests for the A1 and V1 models, and scaling will be done for the A2 and V2 scenarios. Mass point emulation will also be carried out again to reduce the number of reconstructed samples needed. The full Run 2 dataset is expected to be  $\sim 140 \text{ fb}^{-1}$ . To estimate how the limits will improve for such a dataset, the NLO limits obtained with  $36.1 \text{ fb}^{-1}$  have been scaled to an integrated luminosity of  $140 \text{ fb}^{-1}$ . Figure 4.1 shows a projection for the NLO vector limits [21]. This projection assumes the same signal region and background estimates as used for the 2015+2016 dataset. These will of course change with the full dataset, but it gives an estimate for the masses at which we should request samples. Compared to  $36.1 \text{ fb}^{-1}$ , the expected reach in  $m_{\text{med}}$  improves from 550 GeV to nearly 900 GeV for light  $m_\chi$ , and the maximum reach in  $m_\chi$  improves from 250 GeV up to 350 GeV.

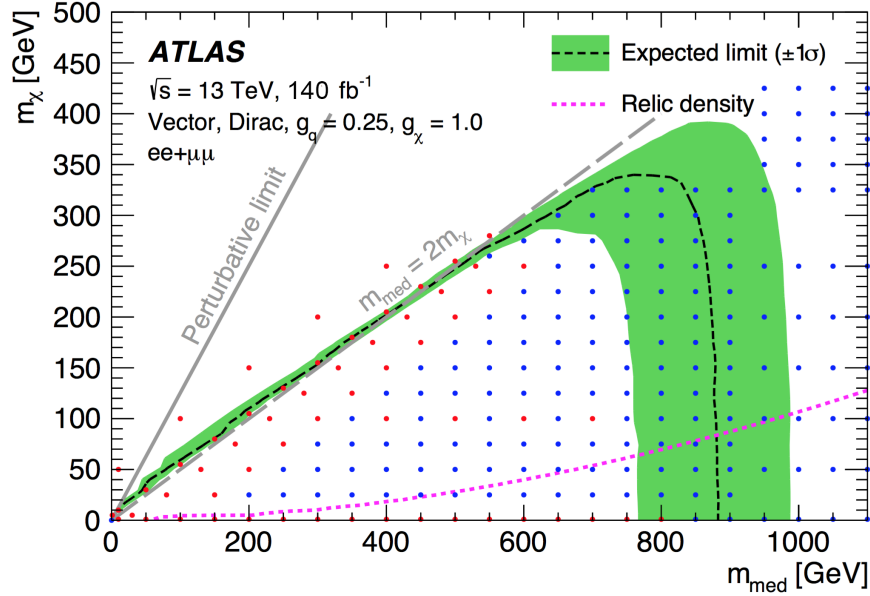


Figure 4.1: Prospective NLO  $s$ -channel vector exclusion limit with  $140 \text{ fb}^{-1}$  [21].

In addition to the simplified models, the 2HDM+PS model has become a new standard in the analysis. A similar projection to  $140 \text{ fb}^{-1}$  will be done using the limits on  $m_H$  vs  $m_a$  and  $\tan \beta$  vs  $m_a$  with  $36.1 \text{ fb}^{-1}$  shown in Section 3.4, and a request for more reconstructed samples will follow suit. Mass point emulation for the 2HDM+PS model is more complicated than for the simplified models; both the signal acceptance and the  $E_T^{\text{miss}}$  shape depend non-trivially on  $m_a$  and  $m_H$ , and the best method for emulating samples is still being investigated.

The other type of signature to be investigated with the full Run 2 dataset is the  $t$ -channel signature with a coloured scalar mediator. There are various models that encompass this type of signature (Figure 4.2 shows the relevant  $t$ -channel diagrams for mono- $Z$ ). A few potential models to be considered are discussed here. These models are of interest for the mono- $Z$  search because the  $Z$  is allowed to couple directly to the mediator, a channel unique to mono- $Z$ .

The Papucci model [23] was the first  $t$ -channel model recommended by the LHC DM WG in Ref. [6]. The interaction Lagrangian is given by:

$$\mathcal{L}_{\text{int}} = g \sum_{i=1,2} \left( \eta_{(i),L} \bar{Q}_{(i),L} + \eta_{(i),u,R} \bar{u}_{(i),R} + \eta_{(i),d,R} \bar{d}_{(i),R} \right) \chi + h.c. \quad (4.4)$$

Here  $Q_{(i),L}$ ,  $u_{(i),R}$ , and  $d_{(i),R}$  are the SM quarks,  $\eta_{(i),L}$ ,  $\eta_{(i),u,R}$ , and  $\eta_{(i),d,R}$  are the mediator particles, and  $g$  is the coupling between the SM particles and dark matter.  $L$  and  $R$  indicate left- and right-handedness, and the index  $i$  is the quark generation. In the Papucci model

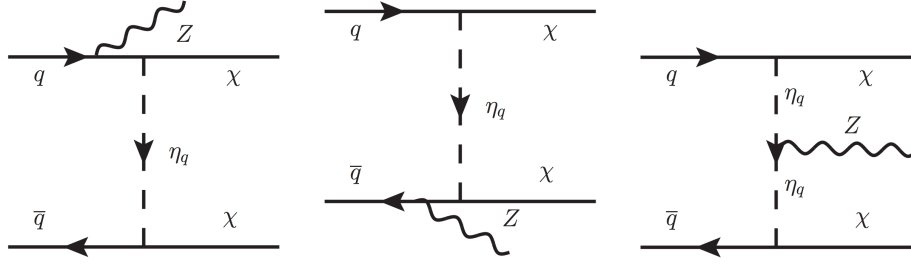


Figure 4.2:  $t$ -channel diagrams with the mono- $Z$  signature [22].

only the first two generations are considered.

The mono-jet analysis recently set limits on the  $t$ -channel signature using the Bell model [22], a variant of the Papucci model with the interaction Lagrangian:

$$\mathcal{L}_{\text{int}} = g \sum_{i=1,2,3} \eta_{(i),L} \bar{Q}_{(i),L} \chi + h.c. \quad (4.5)$$

In this model, couplings to right-handed quarks are turned off, but the third generation of quarks is included. The mono-jet analysis chose to use this model without including the third generation. This decision was based on the availability of Bell et al. to answer technical questions about the implementation/generation in MADGRAPH. The best choice for the mono- $Z$  search will need to be investigated.

The so-called Less Simplified (LS) models [24] are another promising category. These models are similar to simplified models but have the full gauge symmetry of the Standard Model. For this model the interaction Lagrangian between quarks and dark matter for  $t$ -channel processes is:

$$\mathcal{L}_{\text{int}} = - \left[ \bar{\chi} \sum_{i=1,2,3} \sum_{j=1,2,3} \left( \tilde{Q}_L^{i\dagger} (\lambda_{Q_L})_i^j Q_{Lj} + \tilde{u}_R^{i\dagger} (\lambda_{u_R})_i^j u_{Rj} + \tilde{d}_R^{i\dagger} (\lambda_{d_R})_i^j d_{Rj} \right) + h.c. \right] \quad (4.6)$$

In this notation,  $\tilde{Q}_{Li}$ ,  $\tilde{u}_{Ri}$ , and  $\tilde{d}_{Ri}$  are new scalar bosons, partners of the SM particles  $Q_{Li} = (u_{Li}, d_{Li})^T$ ,  $u_{Ri}$ , and  $d_{Ri}$ . Each interaction depends on the chirality, with couplings  $\lambda_{Q_L}$ ,  $\lambda_{u_R}$ , and  $\lambda_{d_R}$ . The dark matter mass  $m_\chi$  is another parameter, along with twelve mediator masses (four for each of the three generations). For searches in  $pp$  collisions, only the first generation will be relevant, so the mediator masses in the second and third generations are approximated to be heavy. With this assumption and a few other simplifications discussed in Ref. [24], the number of free parameters for a first benchmark can be reduced to only four:

two couplings  $\lambda_{Q_L}$  and  $\lambda_{u_R}$ , and two masses  $m_{Q_L}$  ( $= m_{Q_{Lu}} = m_{Q_{Ld}}$ ) and  $m_\chi$ . Hence 2D mass exclusion limits could be set for fixed couplings as a first step.

And there are even more models [25] being considered as potential new  $t$ -channel benchmarks. Discussions are needed with the LHC DM WG in order to determine the best model(s) to investigate.

The Papucci model may serve as a good starting point. The mono- $Z$  analysis currently has eight Papucci model signal samples that were requested at the start of Run 2. Hypothesis tests were run on them with  $36.1 \text{ fb}^{-1}$  of data, but none of the samples were excluded. The mono-jet analysis recently set  $t$ -channel exclusion limits using the Bell model, and their axial-vector and coloured scalar mediators exclusion regions were quite similar. Hence it was unexpected that none of the mono- $Z$  signals were excluded. This led to some investigations, revealing that the mono- $Z$  samples were generated with an incorrect mediator width. The plan now is to use MADGRAPH to generate  $t$ -channel samples with the correct and incorrect mediators to understand the effect on signal. If only the cross section is affected and not the  $E_T^{\text{miss}}$ , then it may be possible to scale the incorrect reconstructed samples to the correct normalization and then rerun the limit setting. From the mono-jet analysis we expect to get similar reach in mass as for the axial-vector model. Then an estimate can be made on how far the limit will reach and a full set of  $t$ -channel samples can be requested. Mass point emulation will also need to be investigated at the same time to determine how fine/coarse the grid of reconstructed points should be. This could be done in tandem with investigating another model, such as the LS model, for which we have already generated our own MC.

## 4.4 Other Analysis Improvements

One improvement on the horizon for the analysis is the inclusion of weights in the official ATLAS signal MC generation to calculate QCD, PDF, and PS systematic uncertainties. This will allow the systematic variations to be calculated for each sample using a weight, rather than having to tediously generate our own truth samples for each variation. This will be especially useful for NLO samples, since MC generation will take much longer than for models at LO. In addition, the uncertainty for each sample will be used rather than having to interpolate between masses, etc. The technical implementation of including these weights in our MADGRAPH and PYTHIA simulation has been successful; the weights will be included in the upcoming NLO simplified model sample requests, and hopefully all future requests for other models. The proper procedure for using these weights will need to be studied and the analysis code will need to be adapted accordingly.

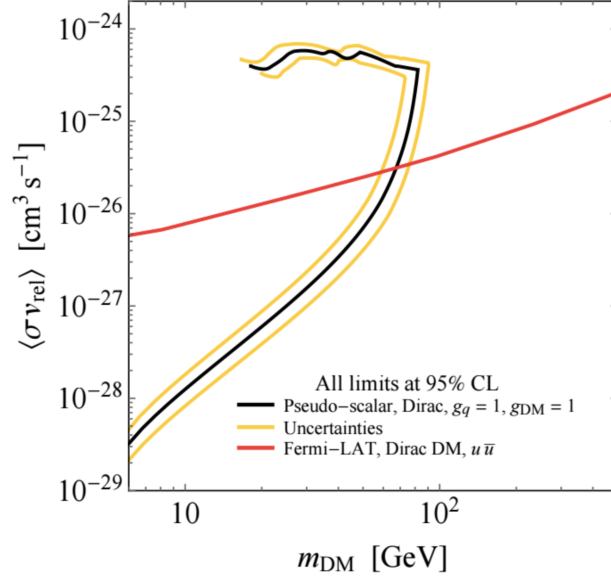


Figure 4.3: Schematic of a collider limit on  $\langle\sigma v_{\text{rel}}\rangle$  overlaid with a ID measurement [3].

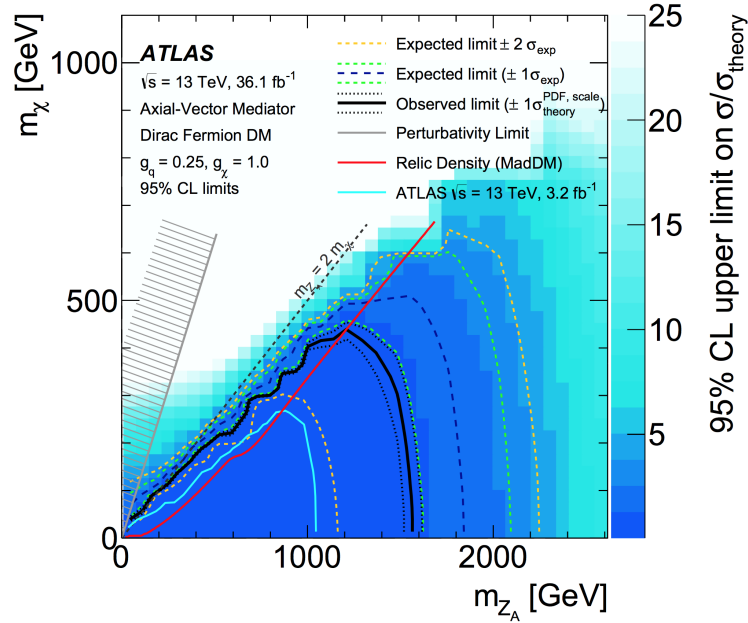


Figure 4.4: Mono-jet axial-vector upper limits on  $\mu$  with  $36.1 \text{ fb}^{-1}$  [26].

There are also a few different interpretations of the mono- $Z$  exclusion limits that remain to be done. For example, the limits have previously been recast into limits on the DM-proton scattering cross section for comparison with direct detection experiments. The same can be done to put limits on the velocity-averaged dark matter annihilation cross section into  $q\bar{q}$  and compare with indirect detection experiments. The procedure for converting the 2D mass



limits into a limit on  $\langle\sigma v_{\text{rel}}\rangle$  is covered in Ref. [3]. Figure 4.3 gives a schematic example of such a comparison.

The mono- $Z$  exclusion limits can also be reinterpreted as an upper limit on the dark matter production cross section. The 2D mass exclusions shown in e.g. Figure 3.5 are determined using the  $\text{CL}_s$  value for a signal strength of  $\mu = 1$ . The observed contour is the line at which  $\text{CL}_s = 0.05$ , and the upper limit on  $\mu$  on this line equals 1 by definition. The region within the contour has an upper limit  $< 1$ , and the region outside the contour has an upper limit  $> 1$ . The upper limit on  $\mu$  can hence be used to determine the upper limit on the cross section for the dark matter production process using  $\mu \equiv \sigma/\sigma_{\text{theory}}$ , where  $\sigma$  and  $\sigma_{\text{theory}}$  are the observed and predicted production cross sections. Figure 4.4 shows such a plot from the mono-jet axial-vector search. The colours on the  $z$ -axis indicate the observed upper limit on  $\mu$ . The same type of plot can be produced for mono- $Z$ .

Finally, the mono- $Z$  analysis software will continue to be used and improved throughout Run 2. With each new data-taking period, there comes new sets of recommendations on how to use the tools for calibrating objects, apply pileup reweighting, etc. These recommendations are being finalized for the 2017 data-taking period, and there will be more to come for 2018. The code will continue to be updated and validated throughout the entire Run 2 campaign.

# Chapter 5

## Conclusions

An overview of the mono- $Z$  search has been presented, including the progress made so far and the work to be done for the full Run 2 analysis. An introduction to the LHC and ATLAS detector is given alongside the theory of dark matter searches at colliders. So far, the mono- $Z$  analysis has set limits on the benchmark  $s$ -channel simplified models and 2HDM+PS models. The analysis involves several aspects, including event selection optimization, background estimation, systematic evaluation, and setting exclusion limits. Previous contributions in these categories are discussed, including the estimation of the  $Z$ +jets background using two different techniques (the ABCD method and the developing  $\gamma$ +jets reweighting scheme), estimation of theoretical uncertainties on the dark matter signal acceptance, and limit setting for the simplified and 2HDM+PS models. There are several improvements to be done for the full Run 2 dataset, projected to contain  $140 \text{ fb}^{-1}$  of data. The most important improvement will be the addition of new models to the analysis, including  $t$ -channel processes unique to the mono- $Z$  search, and the continued pursuit of the 2HDM+PS models. The  $\gamma$ +jets estimation for the  $Z$ +jets background will continue to be developed and finalized, and new variables such as the  $E_{\text{T}}^{\text{miss}}$  significance and particle-flow  $E_{\text{T}}^{\text{miss}}$  will be studied, hopefully leading to improvements in the primary observable of the analysis. Other reinterpretations of the mono- $Z$  exclusion limits will also be investigated. With  $140 \text{ fb}^{-1}$  of data and a variety of models to be studied, the mono- $Z$  search looks promising.

# Appendix A

## Appendix

### A.1 Event Selections

Table A.1 summarizes the event selection requirements from the 2015+2016 dataset and the backgrounds they reduce.

Variable	Requirement	Background reduced
Lepton pair	Exactly one $e^+e^-$ or $\mu^+\mu^-$ pair with leading (subleading) $p_T > 30$ (20) GeV	–
Third lepton	Veto additional leptons with $p_T > 7$ GeV	$WZ$
$m_{\ell\ell}$	76-106 GeV	$WW/Wt/t\bar{t}/Z \rightarrow \tau\tau$
$E_T^{\text{miss}}$	$> 90$ GeV	$Z+\text{jets}$
$\Delta R_{\ell\ell}$	$< 1.8$	$Z+\text{jets}, WW/Wt/t\bar{t}/Z \rightarrow \tau\tau$
$ \Delta\phi(p_T^{\ell\ell}, E_T^{\text{miss}}) $	$> 2.7$	$Z+\text{jets}, WW/Wt/t\bar{t}/Z \rightarrow \tau\tau$
Fractional $p_T$ diff.	$< 0.2$	$Z+\text{jets}$
$E_T^{\text{miss}}/H_T$	$> 0.6$	$Z+\text{jets}$
$b\text{-jets}$	Veto $b\text{-tagged jets}$	$t\bar{t}$

Table A.1: Event selections used for the 2015+2016 dataset.

Several variables are calculated from the lepton pair.  $m_{\ell\ell}$  and  $p_T^{\ell\ell}$  are the invariant mass and the transverse momentum of the pair, and  $\Delta R_{\ell\ell}$  is the angular separation between them, where  $\Delta R = \sqrt{(\Delta\eta)^2 + (\Delta\phi)^2}$ . The fractional  $p_T$  difference =  $|p_T^{\ell\ell} - |\vec{E}_T^{\text{miss}} + \sum \vec{p}_T^{\text{jets}}||/p_T^{\ell\ell}$ , and  $H_T = p_T^{\text{jets}} + p_T^{\ell_1} + p_T^{\ell_2}$ .

## A.2 Calibration Studies on Close-By Jets

Jet calibration studies were done for my ATLAS authorship qualification task. The purpose of this work was to validate the jet calibration performance for  $R = 0.4$  anti- $k_T$  EM-scale jets in close-by environments. Studies were done on the jet response and resolution for calibrated, close-by jets in PYTHIA 8 dijet MC as a function of  $\Delta R_{\min}$ , jet area, and  $f_{\text{Closeby}}$ , variables that are used to assess how close-by a jet is. With minimal jet selections and standard  $\Delta R < 0.3$  truth matching, a significant population of low response close-by jets was observed, primarily at low  $p_T$ . Several categories of low response close-by jets were investigated. Of the categories investigated, the most important sources of low response were jets with a multi-matched truth jet (one truth jet matched to several jets), and jets with a bad truth matching. Ghost truth association was studied as a robust alternative to  $\Delta R$  truth matching, which can break down in very close-by environments. After removing different sources of low response and switching to ghost truth matching, good agreement was seen in the response for close-by jets with small  $\Delta R_{\min}$  compared to more isolated jets. However some low response jets with small area and/or large  $f_{\text{Closeby}}$  remained. Topology and GSC dependence was investigated for these remaining jets, as well as the correlation between  $\Delta R_{\min}$ , area, and  $f_{\text{Closeby}}$ .

# Bibliography

- [1] G. Bertone, N. Bozorgnia, J. S. Kim, S. Liem, C. McCabe, S. Otten, and R. Ruiz de Austri, *Identifying WIMP dark matter from particle and astroparticle data*, [arXiv:1712.04793](#) [[hep-ph](#)].
- [2] T. Marrodán Undagoitia and L. Rauch, *Dark matter direct-detection experiments*, J. Phys. **G43** (2016) 013001, [arXiv:1509.08767](#) [[physics.ins-det](#)].
- [3] G. Busoni et al., *Recommendations on presenting LHC searches for missing transverse energy signals using simplified s-channel models of dark matter*, [arXiv:1603.04156](#) [[hep-ex](#)].
- [4] L. M. Carpenter, A. Nelson, C. Shimmin, T. M. P. Tait, and D. Whiteson, *Collider searches for dark matter in events with a Z boson and missing energy*, Phys. Rev. **D87** (2013) 074005, [arXiv:1212.3352](#) [[hep-ex](#)].
- [5] ATLAS Collaboration, M. Aaboud et al., *Search for an invisibly decaying Higgs boson or dark matter candidates produced in association with a Z boson in pp collisions at  $\sqrt{s} = 13$  TeV with the ATLAS detector*, Phys. Lett. **B776** (2018) 318–337, [arXiv:1708.09624](#) [[hep-ex](#)].
- [6] D. Abercrombie et al., *Dark Matter Benchmark Models for Early LHC Run-2 Searches: Report of the ATLAS/CMS Dark Matter Forum*, [arXiv:1507.00966](#) [[hep-ex](#)].
- [7] M. Bauer, U. Haisch, and F. Kahlhoefer, *Simplified dark matter models with two Higgs doublets: I. Pseudoscalar mediators*, JHEP **05** (2017) 138, [arXiv:1701.07427](#) [[hep-ph](#)].
- [8] G. C. Branco, P. M. Ferreira, L. Lavoura, M. N. Rebelo, M. Sher, and J. P. Silva, *Theory and phenomenology of two-Higgs-doublet models*, Phys. Rept. **516** (2012) 1–102, [arXiv:1106.0034](#) [[hep-ph](#)].

- [9] J. Alwall, M. Herquet, F. Maltoni, O. Mattelaer, and T. Stelzer, *MadGraph 5 : Going Beyond*, JHEP **06** (2011) 128, [arXiv:1106.0522 \[hep-ph\]](#).
- [10] J. C. Collins, D. E. Soper, and G. F. Sterman, *Factorization of Hard Processes in QCD*, Adv. Ser. Direct. High Energy Phys. **5** (1989) 1–91, [arXiv:hep-ph/0409313 \[hep-ph\]](#).
- [11] T. Sjöstrand, S. Ask, J. R. Christiansen, R. Corke, N. Desai, P. Ilten, S. Mrenna, S. Prestel, C. O. Rasmussen, and P. Z. Skands, *An Introduction to PYTHIA 8.2*, Comput. Phys. Commun. **191** (2015) 159–177, [arXiv:1410.3012 \[hep-ph\]](#).
- [12] S. Ask, M. A. Parker, T. Sandoval, M. E. Shea, and W. J. Stirling, *Using gamma+jets Production to Calibrate the Standard Model Z(nunu)+jets Background to New Physics Processes at the LHC*, JHEP **10** (2011) 058, [arXiv:1107.2803 \[hep-ph\]](#).
- [13] G. G. et al., *Another Search for strongly produced supersymmetric particles in final states containing a same-flavour opposite-sign dilepton pair, jets and missing transverse momentum in 13 TeV pp collisions*, Tech. Rep. ATL-COM-PHYS-2016-504, CERN, Geneva, May, 2016. <https://cds.cern.ch/record/2151990>.
- [14] M. Baak, G. J. Besjes, D. Côte, A. Koutsman, J. Lorenz, and D. Short, *HistFitter software framework for statistical data analysis*, Eur. Phys. J. **C75** (2015) 153, [arXiv:1410.1280 \[hep-ex\]](#).
- [15] G. Cowan, K. Cranmer, E. Gross, and O. Vitells, *Asymptotic formulae for likelihood-based tests of new physics*, Eur. Phys. J. **C71** (2011) 1554, [arXiv:1007.1727 \[physics.data-an\]](#), [Erratum: Eur. Phys. J. C73,2501(2013)].
- [16] G. Cowan, *Discovery sensitivity for a counting experiment with background uncertainty*, [https://www.researchgate.net/publication/267783179\\_Discovery\\_sensitivity\\_for\\_a\\_counting\\_experiment\\_with\\_background\\_uncertainty](https://www.researchgate.net/publication/267783179_Discovery_sensitivity_for_a_counting_experiment_with_background_uncertainty).
- [17] CMS Collaboration, A. M. Sirunyan et al., *Particle-flow reconstruction and global event description with the CMS detector*, JINST **12** (2017) P10003, [arXiv:1706.04965 \[physics.ins-det\]](#).
- [18] D. Schaefer, D. M. Portillo Quintero, P. Francavilla, C. M. Macdonald, M. Petrov, and E. Tolley, *Object based Missing Transverse Momentum Significance in the ATLAS Detector*, Tech. Rep. ATL-COM-PHYS-2017-1735, CERN, Geneva, Dec, 2017. <https://cds.cern.ch/record/2294922>.

- [19] M. Backović, M. Krämer, F. Maltoni, A. Martini, K. Mawatari, and M. Pellen, *Higher-order QCD predictions for dark matter production at the LHC in simplified models with s-channel mediators*, Eur. Phys. J. **C75** (2015) 482, [arXiv:1508.05327 \[hep-ph\]](#).
- [20] A. Albert et al., *Recommendations of the LHC Dark Matter Working Group: Comparing LHC searches for heavy mediators of dark matter production in visible and invisible decay channels*, [arXiv:1703.05703 \[hep-ex\]](#).
- [21] C. Anelli Personal communication.
- [22] N. F. Bell, J. B. Dent, A. J. Galea, T. D. Jacques, L. M. Krauss, and T. J. Weiler, *Searching for Dark Matter at the LHC with a Mono-Z*, Phys. Rev. **D86** (2012) 096011, [arXiv:1209.0231 \[hep-ph\]](#).
- [23] M. Papucci, A. Vichi, and K. M. Zurek, *Monojet versus the rest of the world I: t-channel models*, JHEP **11** (2014) 024, [arXiv:1402.2285 \[hep-ph\]](#).
- [24] P. Ko, A. Natale, M. Park, and H. Yokoya, *Simplified DM models with the full SM gauge symmetry : the case of t-channel colored scalar mediators*, JHEP **01** (2017) 086, [arXiv:1605.07058 \[hep-ph\]](#).
- [25] M. Bauer, M. Klassen, and V. Tenorth, *Universal Properties of Pseudoscalar Mediators*, [arXiv:1712.06597 \[hep-ph\]](#).
- [26] A. Collaboration, *Search for dark matter and other new phenomena in events with an energetic jet and large missing transverse momentum using the ATLAS detector: Draft 1.0 for the 2017 monojet paper*, Tech. Rep. ATL-COM-PHYS-2017-716, CERN, Geneva, Jun, 2017. <https://cds.cern.ch/record/2268179>. A draft 0.0 for EB discussion.